

Closed Loop Control of Turbulent Flows

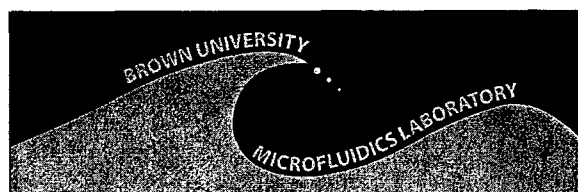
by

Kenneth Breuer



20060306 032

Microfluidics Laboratory
Division of Engineering
Brown University
Providence, RI 02912



October 2005

DISTRIBUTION STATEMENT A
Approved for Public Release
Distribution Unlimited

REPORT DOCUMENTATION PAGE

AFRL-SR-AR-TR-06-0047

Public reporting burden for this collection of information is estimated to average 1 hour per response, including the time for reviewing instructions, searching existing data sources, gathering the data needed, and completing and reviewing this collection of information. Send comments regarding this burden estimate or any other aspect of this collection of information, including suggestions for reducing this burden, to Washington Headquarters Services, Directorate for Information Operations and Reports (0704-0188), 4302. Respondents should be aware that notwithstanding any other provision of law, no person shall be subject to any penalty for failing to comply with a collection of information if it does not have a valid OMB control number. PLEASE DO NOT RETURN YOUR FORM TO THE ABOVE ADDRESS.

1. REPORT DATE (DD-MM-YYYY) 10/02/2005		2. REPORT TYPE Final Report		3. DATES COVERED (From - To) 01/06/02 to 30/09/05	
4. TITLE AND SUBTITLE Closed-Loop Control of Turbulent Flows				5a. CONTRACT NUMBER n/c	
				5b. GRANT NUMBER F49620-02-1-0278	
				5c. PROGRAM ELEMENT NUMBER n/a	
6. AUTHOR(S) Breuer, Kenneth				5d. PROJECT NUMBER n/a	
				5e. TASK NUMBER n/a	
				5f. WORK UNIT NUMBER n/a	
7. PERFORMING ORGANIZATION NAME(S) AND ADDRESS(ES) Brown University Division of Engineering 182 Hope Street Providence, RI 02912				8. PERFORMING ORGANIZATION REPORT NUMBER n/a	
9. SPONSORING / MONITORING AGENCY NAME(S) AND ADDRESS(ES) AFOSR/NA 875 N. Randolph St., Ste 325 Arlington, VA 22203-1768				10. SPONSOR/MONITOR'S ACRONYM(S) AFOSR	
				11. SPONSOR/MONITOR'S REPORT NUMBER(S) n/a	
12. DISTRIBUTION / AVAILABILITY STATEMENT DISTRIBUTION STATEMENT A. Approved for public release; distribution is unlimited.					
13. SUPPLEMENTARY NOTES					
14. ABSTRACT Theoretical modelling and experiments were conducted with a goal towards reducing skin friction in a turbulent channel flow. We developed closed loop adaptive feedforward algorithms, as well as actuators and sensor systems for implementation in a turbulent channel. Significant progress was made in theoretical controller development. Actuators were successfully fabricated and characterized, and open loop performance was demonstrated, although more research is required to complete the closed loop experimental part of the program					
15. SUBJECT TERMS Flow control, Feedforward control, Turbulent Boundary Layers, Drag reduction					
16. SECURITY CLASSIFICATION OF:			17. LIMITATION OF ABSTRACT None	18. NUMBER OF PAGES 46	19a. NAME OF RESPONSIBLE PERSON
a. REPORT unclassified u	b. ABSTRACT unclassified u	c. THIS PAGE unclassified u			19b. TELEPHONE NUMBER (include area code)

This report is the final technical report for the AFOSR award F49620-02-1-0278. Any technical questions should be addressed to *kbreuer@brown.edu*

Contents

Table of Contents	ii
List of Tables	iii
List of Figures	iv
1 Introduction	1
2 Development of Actuator Array	4
2.1 The Water Channel Facility	4
2.2 Shear Stress Sensors	5
2.3 Actuators	5
2.3.1 Non-dimensional Scaling	5
2.3.2 Fabrication	8
2.4 Data Acquisition and Instrumentation	9
2.4.1 Digital Signal Processors (DSP)	9
2.4.2 National Instruments (NI) Data Acquisition	11
2.4.3 Particle Image Velocimetry (PIV)	11
2.5 Results and Discussion	12
2.5.1 Actuator Dynamics	12
2.5.2 Open loop forcing in turbulent channel flow	19
3 Control Theory	24
3.1 Finite Impulse Response (FIR) Filters	24
3.2 Least-Means Squared (LMS) Algorithm	26
3.3 Filtered-X LMS (FXLMS) Algorithm	27
3.4 MATLAB Simulation of Control System	28
3.4.1 DSP Code	29
3.5 Control System Performance	31
4 Conclusions	36
Bibliography	37

List of Tables

2.1	The turbulent scaling dimensions of the flow facility operating at $Re^* = 180$.	5
-----	---	---

List of Figures

1.1	Schematic diagram of the synthetic jet actuator and external flow characteristics. The oscillating membrane is represented on the left, pushing and pulling fluid through the exit slit of the cavity.	2
1.2	The control system is composed of actuators, sensors, and a controller. The downstream sensors provide feedback data to the controller.	2
2.1	A schematic diagram of the turbulent water channel facility at Brown University. The flow rate is controlled by the pressure differential between the upstream and downstream tanks. A pump returns water to the supply tank.	4
2.2	PCB board for hot-wires sensors. Each plate has 4 sensors with center-to-center spacing of 6.35 mm.	5
2.3	A view of the hot-wire shear stress sensors. A 6 μm -diameter Wollaston wire is soldered across the electrodes.	6
2.4	Schematic diagram of the scaling of the actuator array. The actuator slit measures 10 l^* by 160 l^* . The sensors are placed 125 l^* up- and down-stream from the center of the actuator slit exits.	7
2.5	CAD drawing of the design of the actuator speaker mounting plates.	8
2.6	The fabricated actuator speaker mounting plates. The parts were made from 0.010"-dia. ABS plastic thread in a rapid prototyping facility.	9
2.7	Compact audio speakers were used to generate the oscillations inside the actuators. Photo provided by DigiKey Corp.	10
2.8	A CAD view of the exit slit plate.	10
2.9	A schematic diagram of the PIV setup. The PIV controller synchronizes the firing of the lasers and camera.	12
2.10	Velocity measurements at 8 different phases with the actuators operating at 2 V_{P-P} and 60Hz. Wall-normal measurements are shown in (a), while the spanwise is shown in (b). The location of the actuator is indicated by the arrow, just 0.15mm below the field of view. Note that the flow characteristics are largely reversible when comparing the blowing ($0 \leq t \leq 3/8\tau$) and suction ($4/8\tau \leq t \leq 7/8\tau$) portions of the oscillation. The colormap ranges from -2 cm/s to 2 cm/s in the wall-normal direction and from -1 cm/s to 1 cm/s in the spanwise.	13

2.11	The Wall-normal velocity profiles in (a) are taken from Figure 2.10(a) through a horizontal plane 1mm above the actuator. The spanwise velocity profiles in (b) are taken from Figure 2.10(a) through a wall-normal plane located 2mm to the right of the exit slit. The reversibility is apparent as the magnitudes of the velocities are roughly equal.	13
2.12	Velocity measurement at 8 phases in the wall-normal direction. The actuator is operating at 5 V_{P-P} and 60Hz. The dimensions, phases, and location of the actuator are the same as those in Figure 2.10. Note the persistence of a region of upward wall-normal velocity. There is also a lack of spanwise velocity during the blowing portion of the phase ($0 \leq t \leq 3/8\tau$). The colormap in (a) ranges from -7 cm/s to +7 cm/s and in (b) ranges from -4 cm/s to +4 cm/s.	14
2.13	Wall-normal velocity profiles over the 8 phases of Figure 2.12(a). The profiles are taken from a virtual plane 1mm over the actuator operating at the voltage of 5 volts peak-to-peak and a frequency of 60Hz. Spanwise velocity profiles taken from the measurements of Figure 2.12(b) through a wall-normal virtual plane 2 mm to the right of the actuator exit. The actuator is operating at 60Hz and 5 volts peak-to-peak. It can be observed that at certain times during the cycle, there is little X-direction motion(blowing) and, alternately, a large flow to the left(suction).	15
2.14	The wall-normal momentum at the same location as the previous profiles. The reversible and irreversible cases are both evident. The maximum and minimum velocities taken 1mm above the slit exit. The blowing phase produces a higher magnitude velocity than the suction phase.	16
2.15	A velocity measurement of a pair of actuators operating in phase at 60 Hz and with an input voltage of 1 V_{P-P} . The colors range from -2 cm/s to 2 cm/s. The actuator exits are at the bottom of the frame, 0.15 mm below the window frame. The colors represent velocities ranging from -1 cm/s to 1 cm/s.	17
2.16	A velocity measurement of a pair of actuators operating out of phase (180°) at 60 Hz and with an input voltage of 1 V_{P-P} . The dimensions, actuator location, and color mapping are the same as in Figure 2.15.	18
2.17	The wall-normal velocity at 8 phases of a pair of actuators operating in phase at 5 V_{P-P} and 60 Hz. The colors ranges from -8cm/s to 8cm/s. The dimensions and actuator location are the same as Figure 2.15.	18
2.18	The wall-normal velocity of a pair of actuators operating out of phase at 5 V_{P-P} and 60 Hz. The dimensions and actuator location are the same as Figure 2.15. The colors ranges from -8cm/s to 8cm/s. The colors ranges from -4cm/s to 4cm/s. The dimensions and actuator location are the same as Figure 2.15.	19
2.19	The baseline channel flow. Mean streamwise velocity is shown in (a). Fluctuations in (b) confirm that the turbulent flow is well-developed.	20
2.20	A PIV measurement streamwise velocity of the baseline channel flow. The colors ranges from 0 to 12cm/s($u^+ = 15$).	21

2.21	Figures (a) - (d) show streamwise velocity at various spanwise locations of the channel flow during actuator operation at $5 V_{P-P}$ and 60 Hz. Dimensions are identical to those of Figure 2.20. The colors range from 0 to 9cm/s. The inset is a schematic of the vorticity formed by the actuator.. Examining the different spanwise locations, the actuator has little effect on the channel flow at $z^* = 50$ (a), the downward portion of the synthetic jet can be seen at $z^* = 34$ (b). The upward momentum can be clearly seen at $z^* = 17$, (c), and $z^* = 0$, (d).	21
2.22	Velocity profiles of the channel flow comparing actuated and non-actuated cases averaged over the streamwise direction. The data is acquired from the field of view in Figure 2.20. The actuator effect can be seen and is largely dependant on amplitude. The actuator is pushing lower speed fluid upward. Note that the effect is largely independent of actuator phase.	22
2.23	Shear stress measurements showing the downstream effect of the actuators at various voltages and frequencies. Negative deviations indicate a slowdown of the flow over the sensor.	23
3.1	Conceptual view of FIR filtering as the weighted sum of past input values. .	24
3.2	The LMS Algorithm requires data from both the input and the output to improve its performance.	26
3.3	The Filtered-X LMS Algorithm compensates for the system dynamics, C , by adding an additional filter, C^* , to the input that approximates the dynamics of the system.	27
3.4	The LMS system was implemented using MATLAB Simulink.	28
3.5	The LMS portion of the simulation is shown.	28
3.6	Simulink Simulation of a 1-channel FXLMS filter	29
3.7	The multichannel FXLMS. Note that there is only one error signal and one output signal.	30
3.8	In addition to the error path response, there are phase delays in the reference signal path, in our case the flow dynamics between the upstream sensors and the actuator.	30
3.9	The environment block used to simulation the nonlinearities of the turbulent flow.	30
3.10	The product of the simulation phase of the experiment was a DSP programmed to receive input from three upstream sensors and one downstream sensor to control each actuator.	31
3.11	The performance of the LMS simulation with a combination Gaussian and sine wave inputs with a range of μ values. Starting at $\mu = 0.01$, the RMS does not change significantly since the coefficient adjustments are very small. As μ increases, the RMS decreases until $\mu = 0.5$, and then the performance worsens until $\mu = 2.1$, when the RMS increases from its initial value.	32
3.12	The stability of the LMS algorithm is vulnerable to delays in the error path.	33

3.13	The 500-sample RMS of the error signal of the FXLMS MATLAB simulation, using the same input signal and filter variables of $\mu = 0.1$ and 64 taps, with downstream delays of 0, 1, 2, 3, and 50 samples. The FXLMS is successful in adapting to all of the cases.	33
3.14	The effect of delays between the upstream sensor on the performance of the algorithm. Note that for delays of 50 and 60 samples, the filter is unable to filter the noise signal. The 64-tap filter does not have the capacity to store the delay and the necessary coefficients.	34
3.15	The effect of simulated system nonlinearities on the RMS of the error output. The system grows more unstable as nonlinearity increases. However, as the number of channels is increased, the variance of the system error (output) is decreased.	35

Chapter 1

Introduction

The Synthetic Jet actuator has received considerable attention over the past several years as a good candidate for flow control applications. Its compact nature, ability to generate momentum without the need for fluidic plumbing, and potential for introducing unsteadiness into a larger-scale flow contribute to its attractiveness for use in active control applications. The current experiments were designed to judge the practicality of this approach. The device was first described in some detail by Ingard [8], but re-discovered, developed, and applied to problems in flow control by Glezer and co-workers [19, 20, 4]. The fluidic jet is created by the periodic forcing of a cavity by means of a piston or membrane (Figure 1.1). The forcing alternately blows and sucks fluid through a small orifice generating a jet in the ambient flow during the compression stroke, followed by a sink flow during the suction stroke. If the jet Reynolds number is sufficiently large, the fluid will separate from the orifice lip and form a coherent jet into the fluid above. However, the suction cycle, no matter how high the Reynolds number, will resemble a point sink flow. Thus, for sufficiently high amplitudes, an asymmetric, directed flow is established, creating a point source of momentum, with no net mass injection. Such actuators have been explored for use in a variety of flow control applications, including separation control [12, 7, 18], control of jets [20], and small scale control of turbulence [15, 16, 10].

The current experiments are motivated by the somewhat unusual application of near wall flow control for the purposes of achieving distributed control of turbulent boundary layers. Previous work done by Rathnasingham and Breuer [16] demonstrated the successful application of these actuators using a series of linear filters in reducing turbulent streamwise velocity fluctuations. The purpose of the experiments described here was to build upon this work by increasing the number of actuators, implementing an adaptive control scheme, and integrating them together to create a real-time control system (Figure 1.2). The particular demands of the channel flow - the velocity, frequency, and size constraints - form an additional layer of design constraints that mandate the use of actuators in a somewhat unusual parameter regime.

Two distinct aspects of the experimental setup will be discussed. First, the physical components of the system, specifically the actuators and sensors, were designed, fabricated and tested. Chapter 2 outlines the engineering of those components. Second, a control theory able to adapt to a turbulent channel flow in real-time was designed using MATLAB

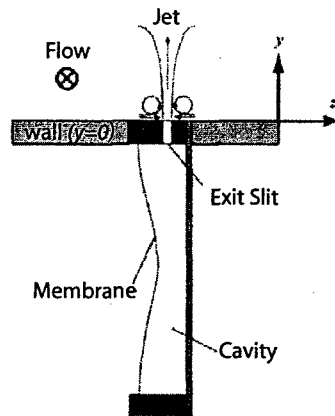


Figure 1.1: Schematic diagram of the synthetic jet actuator and external flow characteristics. The oscillating membrane is represented on the left, pushing and pulling fluid through the exit slit of the cavity.

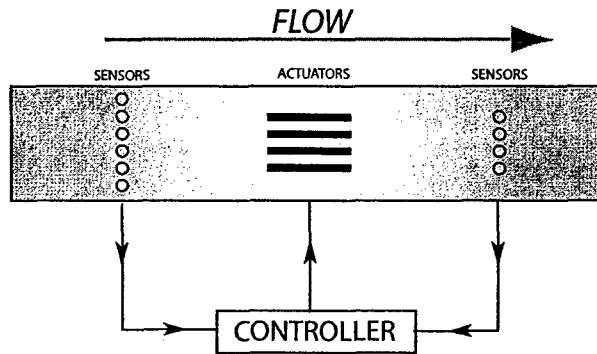


Figure 1.2: The control system is composed of actuators, sensors, and a controller. The downstream sensors provide feedback data to the controller.

simulations. The results are presented in Chapter 3.

Chapter 2

Development of Actuator Array

2.1 The Water Channel Facility

Experiments were conducted in a water channel, shown in Figure 2.1, with cross-sectional dimensions of 4.5 cm ($\sigma = 2.25$ cm) high and 91 cm wide. The flow is driven by the gravity head developed in the upstream tank, and moderated by a back-pressure tank downstream of the test section. The test section is 1 meter long in the streamwise direction, and is preceded by 3 meters of channel in order to ensure fully developed turbulent flow. The water in the downstream tank is returned to the upstream tank by a bank of pumps. Valves are employed for incremental control of the flow rate up to $25,000 \text{ cm}^3/\text{s}$. Since we will argue that the turbulent scaling of the flow dictates the dimensions and operating range of the actuators, the channel was run at a single flowrate, outlined in Table 2.1.

The flow facility at Brown University, at a flowrate of $6000 \text{ cm}^3/\text{s}$, is a low-Reynolds number ($Re^* = 180$) turbulent water channel, with a the friction velocity, u_τ , of approximately 0.8 cm/s. The turbulent length scale, $l^* = \nu/u_\tau$ is $125 \mu\text{m}$ and the turbulent timescale, $t^* = \nu/u_\tau^2$, is 16 ms. Consequently, the frequency scaling factor, f^* , is 62 Hz.

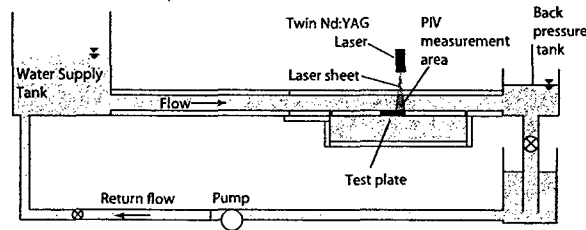


Figure 2.1: A schematic diagram of the turbulent water channel facility at Brown University. The flow rate is controlled by the pressure differential between the upstream and downstream tanks. A pump returns water to the supply tank.

variable	value
u_τ	0.8 cm/s
l^*	125 μm
t^*	16 ms
f^*	62 Hz

Table 2.1: The turbulent scaling dimensions of the flow facility operating at $Re^* = 180$.

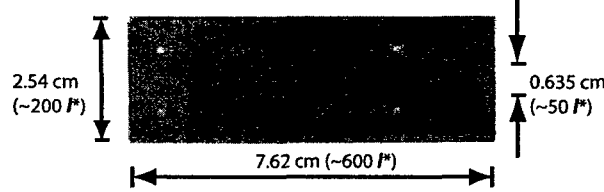


Figure 2.2: PCB board for hot-wires sensors. Each plate has 4 sensors with center-to-center spacing of 6.35 mm.

2.2 Shear Stress Sensors

Flush-mounted hot wires, driven by constant temperature anemometers, were used to measure changes in the local wall shear stress of the channel at locations both upstream and downstream of the actuators [2]. The custom anemometers featured variable gain amplifiers, variable-cutoff low- and high-pass filters, and a built in oscillator for frequency response adjustments. The sensor plates were designed using a PCB circuit layout program and were manufactured on a 2-layer 1/16"-thick printed circuit board material (Figure 2.2). The sensor wire, 6 μm -diameter Wollaston wire, is pictured in Figure 2.3. The wire is soldered across electrodes spaced 0.1 inches (20 l^*) apart and are oriented in the spanwise direction. The sensors were then coated in polyurethane to form an insulating layer and tested for sensitivity and longevity before being installed into the actuator array.

2.3 Actuators

2.3.1 Non-dimensional Scaling

The operation of the actuators can be described with a number of non-dimensional parameters. The relative importance of viscous effects and unsteady effects are two critical parameters. The Reynolds number, Re , is defined by the velocity of the jet and the orifice width:

$$Re = \frac{U_j h}{\nu} \quad (2.1)$$

where U_j is the exit stream velocity, h is the orifice width, and ν is the viscosity. Defined

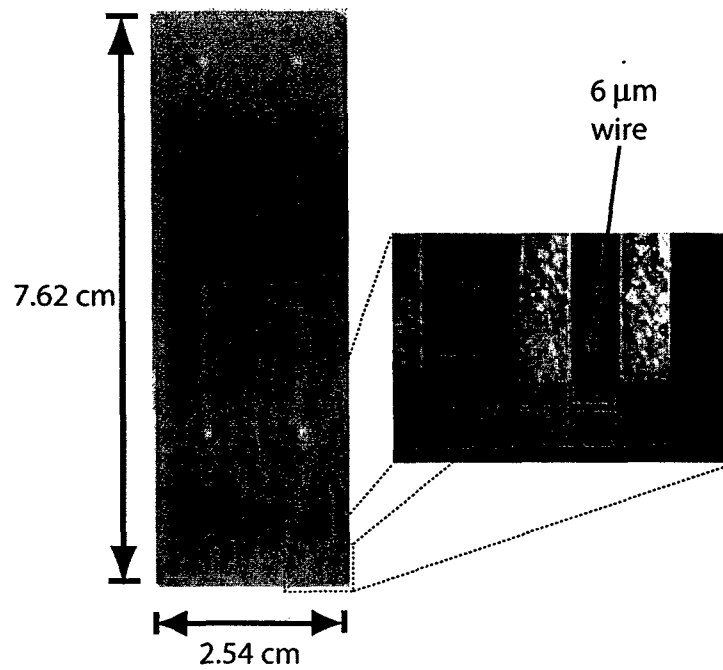


Figure 2.3: A view of the hot-wire shear stress sensors. A $6\text{ }\mu\text{m}$ -diameter Wollaston wire is soldered across the electrodes.

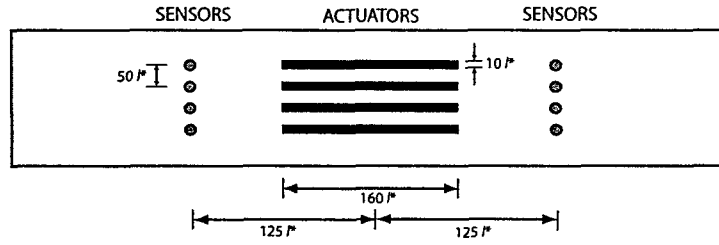


Figure 2.4: Schematic diagram of the scaling of the actuator array. The actuator slit measures $10 l^*$ by $160 l^*$. The sensors are placed $125 l^*$ up- and down-stream from the center of the actuator slit exits.

in this way, the Reynolds number has a very clear physical meaning. In particular, if the Reynolds number falls below approximately 50, the “jet” will not separate from the orifice edge and the flow will become reversible with the blowing phase identical and opposite to the suction phase. The unsteady effects of the system are best described by the Stokes number, St :

$$St = \frac{\omega h^2}{\nu} \quad (2.2)$$

where ω is the operating frequency. The Stokes number contrasts the thickness of the unsteady boundary layer with the size of the orifice. If St is large, the orifice is not strongly influenced by viscous effects. If St is small, the orifice is strongly viscous, and the jet will be suppressed by the boundary layer.

Additionally, the ratio of the Reynolds and Stokes number, known as the Strouhal number, Str , can be examined to evaluate the system:

$$Str = \frac{St}{Re} = \frac{\omega h}{U_j} \quad (2.3)$$

The Strouhal number compares the operating frequency to the typical time it takes a fluid element to advect through the orifice zone. Large Strouhal numbers indicate that the actuator cycles several times before a fluid element manages to pass through the orifice region, while small Strouhal numbers indicate that the fluid elements pass through the orifice in one cycle. The majority of synthetic jets studied operate at relatively high Reynolds numbers and relatively low Strouhal numbers, as this tends to yield strong jets with high directivity and low viscous losses. However, a different regime was implemented in this design for this particular application.

For the case of turbulent flow control, there are some rather unique constraints that the actuator must satisfy. Near wall flow control using blowing and suction has been demonstrated both computationally [3, 1], using massive arrays of idealized blowing and suction, and, in a far more limited (but realistic) way, experimentally [15, 16]. Those investigations have indicated that, in order to be effective, the velocity emitted by the actuator, U_j , should be on the same order as u_τ , or typically about 5% of the free stream velocity. Velocities far higher than this will simply “blow through” the boundary layer and will not be effective

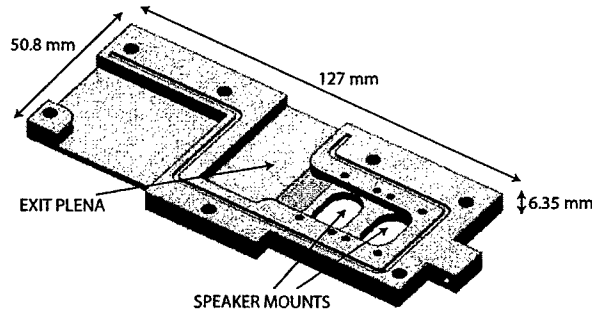


Figure 2.5: CAD drawing of the design of the actuator speaker mounting plates.

for near wall control. In order to minimize the hydraulic roughness of the surface, the exit diameter of the actuator should not be so large so that it represents an unacceptably large hole on the surface. For this, we require that the synthetic jet exit, h , be no more than approximately $10 l^*$, where l^* is the characteristic turbulent length scale, defined as $l^* = \nu/u_\tau$ and ν is the kinematic viscosity. Using these characteristic scales to calculate a jet Reynolds number yields a value of 10, which is right at (or below) the threshold of non-reversible operation. The transition from a reversible source-sink to a directed synthetic jet depends on the separation of the jet from the exit lip on the out-stroke, which will not occur below a Reynolds number of about 10-50. Additionally, the slit length was set to approximately $160 l^*$ and the center-to-center spacing of the slits were set to $50 l^*$ and the layout is outlined in Figure 2.4.

A second issue in the design of the wall-bounded flow control actuator is the operating frequency. Broadly speaking, there are two options of the actuation frequency for a control jet. First, the actuation frequency can coincide with an instability in the larger flow, such that the unsteadiness of the jet is deliberately leveraged in the control scheme. This has been demonstrated very effectively in the case of separation control [17, 18]. the alternative is to drive the actuator jet at a frequency much higher than anything the embedding flow is responsive to. In this case, the unsteadiness of the actuator becomes quickly damped out, and the actuation is quickly reduced to an effectively constant flux jet that does not contain dynamically significant fluctuations. This mode of operation was used by Rathnasingham and Breuer [15, 16], who utilized a synthetic jet actuator operating at a non-dimensional frequency of approximately $f^* f \nu / u_\tau^2 = 1$. In their case, the experiment was in air, and the dimensional frequency was approximately 2 kHz. The advantage of this mode is that the actuator affects the larger flow independently of its internal operating frequency.

2.3.2 Fabrication

The small actuator spacing, the amount of force required to generate adequate jetting, and the underwater operation of the array posed design hurdles that were best met by developing

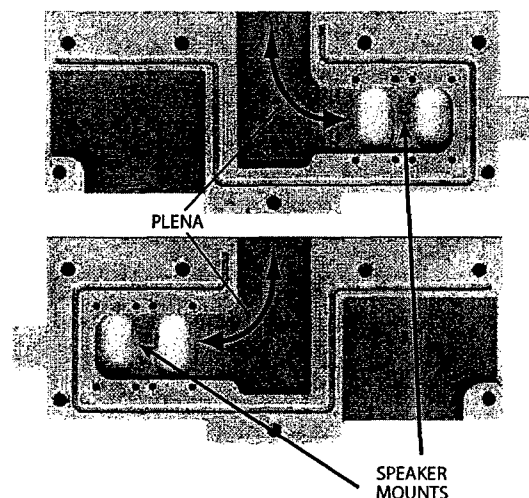


Figure 2.6: The fabricated actuator speaker mounting plates. The parts were made from 0.010"-dia. ABS plastic thread in a rapid prototyping facility.

a custom design utilizing computer-aided design (CAD) tools. Efficient packing was achieved while also meeting the size and fluid velocity requirements. A CAD view of the speaker mounting plate can be seen in Figure 2.5. The plates were built from 0.01"-diameter ABS plastic thread using a Stratasys rapid prototyping machine, and are pictured in Figure 2.6. Mounting holes were threaded and gasket material was used to minimize leaks. Pictured in Figure 2.7 is the low-profile audio speaker, manufactured by CUI Stack, used to generate the flow oscillations. Pairs of these speakers were mounted alternately to the left and right of the exit plenum for space-efficient stacking. The speakers were coated with liquid electrical tape, a flexible waterproof material, to ensure that the speakers would operate underwater. Once the speakers were installed and the plates mounted together, the exit slit was installed in two stages. In order to provide the same thickness as the sensors, a milled fiberglass plate was mounted directly to the actuator plates. Slits were milled into stainless steel 0.003"-thick shim stock by an EDM facility to guarantee a high-precision, consistent exit geometry. The width of the PCB slits is larger than those of the shim stock to create a very sharp exit geometry. The array of actuators was then installed in a flat plate and the shear sensors were attached. To complete the setup, any surface roughness caused by assembly fitting or exposed screws was filled with a waterproof filler material.

2.4 Data Acquisition and Instrumentation

2.4.1 Digital Signal Processors (DSP)

DSPs were used to generate the input signals for the actuators. The systems used were Innovative Integration, Model M44 DSPs, employing 32-bit floating point 60 MHz Texas

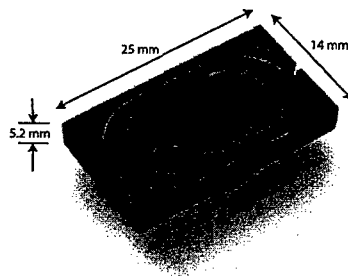


Figure 2.7: Compact audio speakers were used to generate the oscillations inside the actuators. Photo provided by DigiKey Corp.

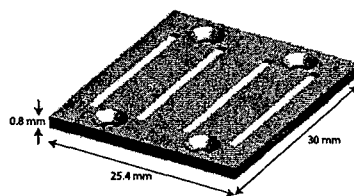


Figure 2.8: A CAD view of the exit slit plate.

Instruments TMS320C44 core processors, each equipped with one A4D4 module. Each A4D4 module adds four 16-bit A/D Channels and four 16-bit D/A Channels. For open-loop operation (non-adaptive) experiments, the DSPs were used to generate sinusoidal waves and the necessary timing signals to trigger the data acquisition systems. For these experiments, a single M44 system was able to address four actuators, each with an independent frequency, amplitude, and phase-delay. Additionally, the DSPs were used in an adaptive, closed-loop application. Each board, sampling 4 channels of sensor data at 250 Hz, was responsible for a single actuator, computing multiple finite impulse response filters and generating new coefficients in real-time (see Chapter 3).

2.4.2 National Instruments (NI) Data Acquisition

Data was acquired using a National Instruments PCI-6052E multifunction data acquisition system. The system features 16 analog inputs and two 16-bit analog outputs, and is able to sample at 333kHz. Data acquisition using these boards was done through MATLAB. In order to capture the dynamics of the flow, the system was set to oversample the Nyquist rate of the turbulent scaling frequency, f^* . The power spectral density of sensor data sampled at 250 Hz indicated adequate oversampling to capture the major component dynamics of the turbulent flow. The autocorrelation also dictated the minimum number of samples needed, while sampling larger time periods decreased measurement uncertainty.

2.4.3 Particle Image Velocimetry (PIV)

ProVision PIV software, distributed by Integrated Design Tools, Inc. (IDT), was used for measurements of the streamwise and wall-normal velocity. Velocity vectors of the flow can be computed from particle displacement in pairs of images. PIV relies on two stages, image acquisition and vector calculation. For image acquisition, a New Wave Solo III 15mW Nd-YAG twin 532-nm laser was used to illuminate the flow field, and 8-bit gray-scale images were captured using a 1360 by 1024-pixel resolution camera (Figure 2.9). Cylindrical and spherical laser optics were used to reshape the laser output in order to illuminate the focal plane of the camera. The field of view in the channel was roughly 20 mm ($160 l^*$) in the streamwise direction, x , and 16 mm ($128 l^*$) in the wall-normal direction, y . The laser and camera timing is handled by a computer-controlled National Instruments PCI-6602E data acquisition board, and the time interval between images ranged from 300 μs to 500 μs . Measurements in the spanwise direction, z , were taken by traversing both the laser and camera.

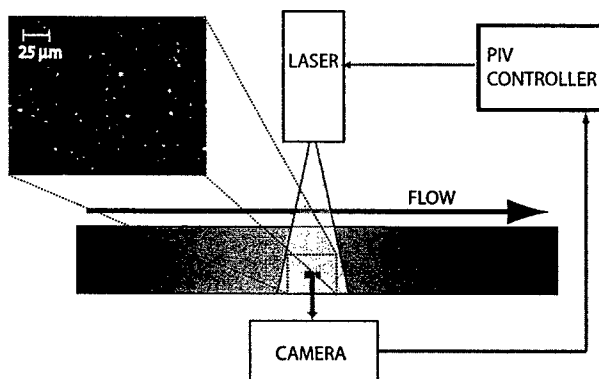


Figure 2.9: A schematic diagram of the PIV setup. The PIV controller synchronizes the firing of the lasers and camera.

2.5 Results and Discussion

2.5.1 Actuator Dynamics

Single Actuator

The actuators were tested using PIV techniques in a small water tank with no mean flow. Only the near field of the actuator was imaged, with a field of view of 7.53mm by 9.78mm. The images were phase-locked to the actuator motion and data was acquired at twenty four phases during a cycle.

Figures 2.10(a) and (b) show the vertical and spanwise velocity, respectively, of a single actuator operating at 60 Hz and a voltage of 2 V_{P-P} . Eight equally-spaced phases of the operation cycle are shown. The actuator position is indicated by the arrow, approximately 0.15 mm below the image in the center. At this low amplitude, the actuator is operating in the reversible mode ($Re = 20.0$, $St = 60$, $Str = 3$), and the vertical (wall-normal) velocity clearly shows a blowing phase ($0 \leq t \leq 3/8\tau$), followed by a suction phase ($4/8\tau \leq t \leq 7/8\tau$) with approximately similar amplitudes and shapes. Similarly, the spanwise velocity shows roughly symmetric motion away from and towards the actuator slit during the respective suction and blowing phases of the cycle.

The wall-normal velocity profiles, $w(x)$, measured 1 mm above the face of the actuator are shown in Figure 2.11(a) for the eight phases shown in Figure 2.10(a). It is apparent that the flow at this operating parameter is reversible. The shape and magnitude of the profile at maximum blowing has a similar shape and magnitude as the profile from the point of maximum suction. Profiles were taken from the phases shown in Figure 2.10(b) through a vertical plane at a distance of 2 mm right of the center of the exit slit, and are shown in Figure 2.10(b). The flow appears reversible as the profiles again exhibit similar magnitude and shape at the points of maximum suction and blowing.

Figure 2.12 shows the same actuator, with the same view and operating frequency, but this time at a voltage of 5 V_{P-P} . At this amplitude and frequency, the Reynolds number is 80, the Stokes number is 60 and the Strouhal number is 0.75. A marked change in the

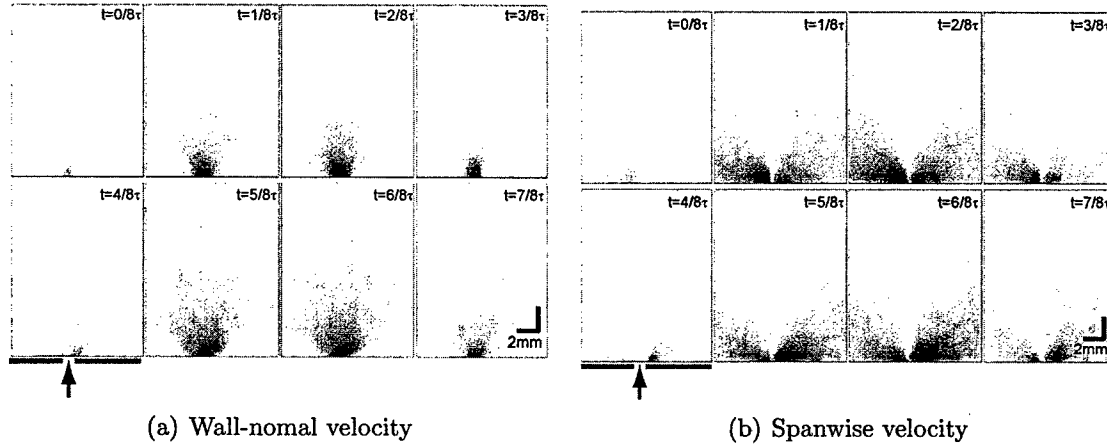


Figure 2.10: Velocity measurements at 8 different phases with the actuators operating at $2 V_{P-P}$ and 60Hz. Wall-normal measurements are shown in (a), while the spanwise is shown in (b). The location of the actuator is indicated by the arrow, just 0.15mm below the field of view. Note that the flow characteristics are largely reversible when comparing the blowing ($0 \leq t \leq 3/8\tau$) and suction ($4/8\tau \leq t \leq 7/8\tau$) portions of the oscillation. The colormap ranges from -2 cm/s to 2 cm/s in the wall-normal direction and from -1 cm/s to 1 cm/s in the spanwise.

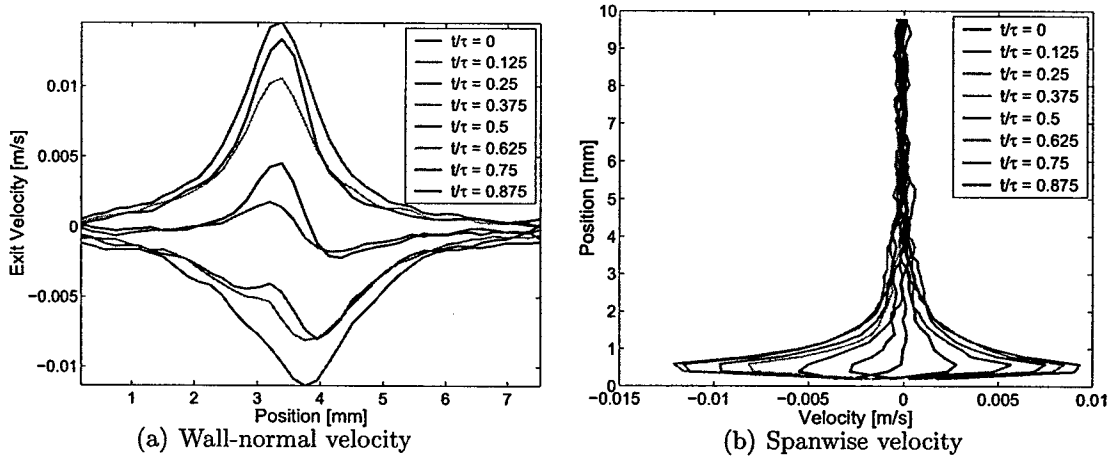


Figure 2.11: The Wall-normal velocity profiles in (a) are taken from Figure 2.10(a) through a horizontal plane 1mm above the actuator. The spanwise velocity profiles in (b) are taken from Figure 2.10(a) through a wall-normal plane located 2mm to the right of the exit slit. The reversibility is apparent as the magnitudes of the velocities are roughly equal.

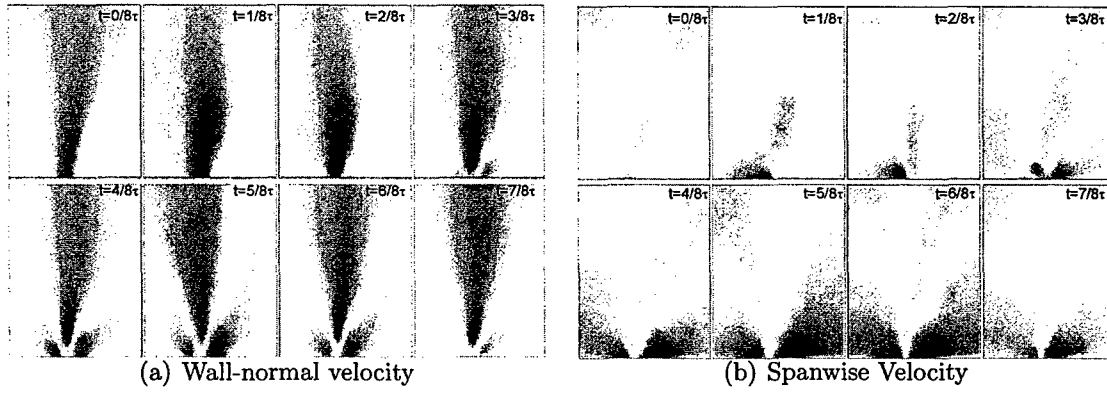


Figure 2.12: Velocity measurement at 8 phases in the wall-normal direction. The actuator is operating at $5 V_{P-P}$ and 60Hz. The dimensions, phases, and location of the actuator are the same as those in Figure 2.10. Note the persistence of a region of upward wall-normal velocity. There is also a lack of spanwise velocity during the blowing portion of the phase ($0 \leq t \leq 3/8\tau$). The colormap in (a) ranges from -7 cm/s to +7 cm/s and in (b) ranges from -4 cm/s to +4 cm/s.

actuator performance is observed, particularly in the wall-normal component. Although the blue side lobes characteristic of the suction phase are still present, they extend more prominently out and upward. This is not surprising since the amplitude is larger. However, the positive velocity component has a strikingly different character from the low-amplitude case. The proportion of the positive-velocity region is much more narrow - indicating that the fluid flow is clearly separating from the exit orifice during the blowing phase, establishing a jetting effect. What is more interesting, however, is that the region of positive velocity persists throughout the cycle. Although weaker, it is still present at the peak of the suction phase. Also, there is no evidence of discrete vortices rising from the actuator exit as has been observed in previous synthetic jet simulations and experiments [19, 11]. The reason for this difference comes from the non-dimensional parameter range in which the current jets operate. The low Reynolds number confirms the dominance of viscous effects such that any directed jet that does form is only barely viable. The high Strouhal number and *very* high Stokes number imply that the actuator driver (i.e. the speakers) cycles many times compared to the time it takes a fluid element to travel through the neck, and consequently there is no room for discrete vortex formation. The net result is a jet that forms a DC source of momentum almost immediately upon formation, rather than at a far distance from the actuator exit, as is the case in similar devices that operate at higher Reynolds numbers. This is precisely the desired effect for the turbulence control application.

The wall-normal velocity profiles measured 1 mm above the slit of the actuator are shown in Figure 2.13(a) for the eight phases shown in Figure 2.12(a). The evolution of the blowing and suction phases are clear, as well as the persistence of a blowing component even at the height of the suction phase. Although there is some asymmetry, for the most part the actuator output is quite symmetric. The spanwise velocity profiles, seen in Figure

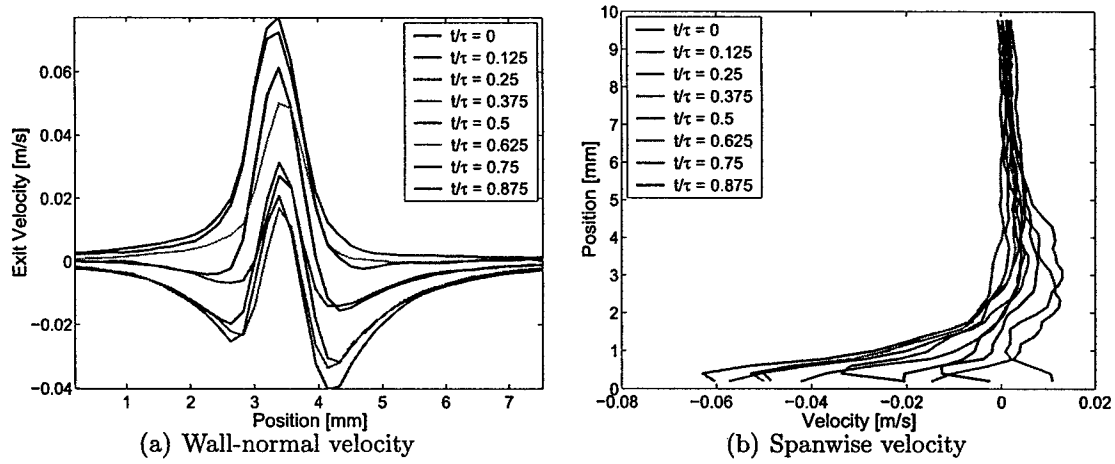


Figure 2.13: Wall-normal velocity profiles over the 8 phases of Figure 2.12(a). The profiles are taken from a virtual plane 1mm over the actuator operating at the voltage of 5 volts peak-to-peak and a frequency of 60Hz. Spanwise velocity profiles taken from the measurements of Figure 2.12(b) through a wall-normal virtual plane 2 mm to the right of the actuator exit. The actuator is operating at 60Hz and 5 volts peak-to-peak. It can be observed that at certain times during the cycle, there is little X-direction motion (blowing) and, alternately, a large flow to the left (suction).

2.13(b), again demonstrate the irreversible behavior of the actuator. The suction phase can be identified since there is a significant negative spanwise velocity close to the exit slit, but during the blowing phases, there is significantly less lateral velocity, indicative of the jetting characteristics.

We can integrate the momentum crossing this surface, shown in Figure 2.14(a) for three different amplitudes, a low voltage (reversible) case (seen in Figure 2.10), an intermediate case, and the high voltage case seen in Figures 2.12. As expected, the low-amplitude case shows complete reversibility with equally sized blowing and suction phases. The intermediate case has transitioned to a directed mode of operation with a strong blowing phase and a very weak suction phase. The high amplitude case continues this trend with very forceful blowing and weaker, but nevertheless significant, negative momentum transfer during the suction phase. We should note that there is additional vertical momentum transfer due to oblique motion below the plane of integration which has not been included in this simple evaluation.

Figure 2.14(b) shows the minimum and maximum velocities measured as functions of voltage for three different operating frequencies. One might expect, for a fixed voltage, the velocity to rise as the frequency increases since the driving velocity might be plainly modeled as $U_j \approx \omega V$, if one were to assume the speaker responds linearly to applied voltage and frequency. However, this is not observed, and in fact the opposite behavior is seen. The velocity drops as the frequency rises. This is likely due to the particular response of the driving speakers. The speakers are audio speakers and were chosen for their compact size.

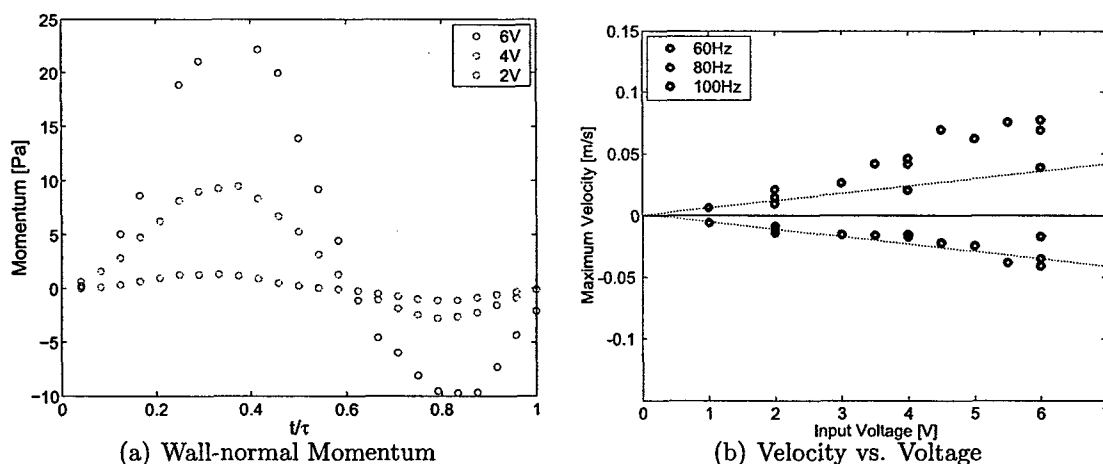


Figure 2.14: The wall-normal momentum at the same location as the previous profiles. The reversible and irreversible cases are both evident. The maximum and minimum velocities taken 1mm above the slit exit. The blowing phase produces a higher magnitude velocity than the suction phase.

They are not designed to operate either at the low frequencies of this application (at the very limit of low-frequency hearing), nor in an aqueous environment. As a result, they are not designed to have a high mechanical impedance. Consequently, the net driving of the cavity weakens with rising frequency, and the jet velocity decreases. The suction velocity scales approximately linearly with the driving voltage, confirming that the suction phase is dominated by an inviscid, linear sink flow. In contrast, the maximum velocity initially tracks the suction velocity (shown as a dotted line, mirrored in the $U = 0$ axis). However, as the voltage increases, the blowing velocity rises supra linearly as the directed motion operation becomes established.

Actuator Pairs

For active control operations, arrays of actuators are needed, and it is of interest to see how actuators interact with each other. It has been demonstrated [21] that two adjacent jets operating together can produce a single jet with increased strength. More interestingly, when operated out of phase, they can generate a vectored jet. However, although there are similarities to the conditions considered by Smith [21], such as the overall geometric arrangement, the application of an array of synthetic jets to distributed wall turbulence control conforming to the constraints discussed above place the actuators in a different operating regime, that of high Reynolds and Stokes numbers. Thus the interacting physics has different characteristics. In addition, for distributed control, it is desirable for the actuators to have negligible influence each other so that they can be included in a linear control system with minimal complexity.

PIV measurements indicate that actuators stacked in an array have a strong influence on each other, even at low amplitudes. In Figure 2.15, two actuators are operating at identical

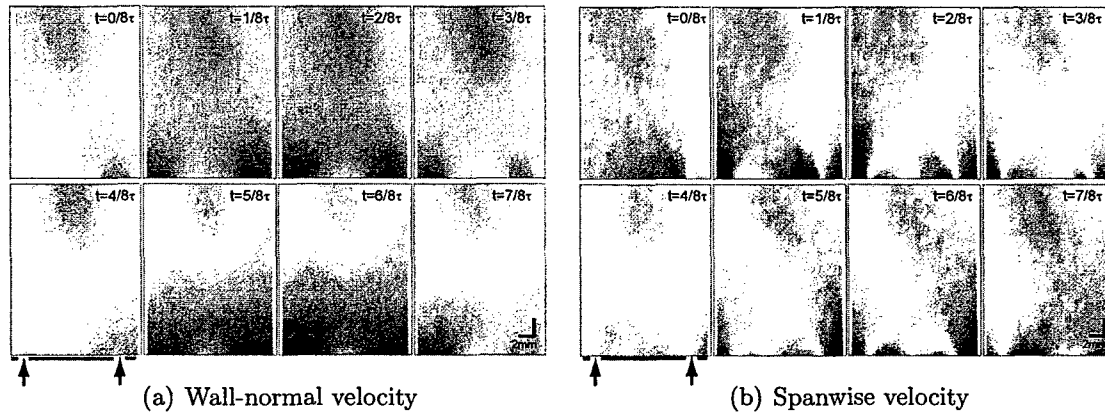


Figure 2.15: A velocity measurement of a pair of actuators operating in phase at 60 Hz and with an input voltage of $1 V_{P-P}$. The colors range from -2 cm/s to 2 cm/s. The actuator exits are at the bottom of the frame, 0.15 mm below the window frame. The colors represent velocities ranging from -1 cm/s to 1 cm/s.

amplitude, frequency, and phase. Although synthetic jetting does not occur, a region of upward velocity appears between the actuators and persists throughout the operating cycle.

Figures 2.15 and 2.16 show the velocity fields in the wall-normal and spanwise directions for a pair of actuators, separated by 6.35 mm. The actuators are operating at low amplitude (in the reversible regime) and are driven with zero-degree phase separation and 180 degrees phase separation, respectively. In this weak forcing case, the separation between the actuators is sufficiently large compared to the slit size and the actuators basin of influence that they operate independently of each other. The overall effect appears to be simply a superposition of the individual velocity characteristics of each actuator. This is ideal for control purposes, but the reversible nature of the actuation might lead to ineffectual control authority - an issue to be determined in the next phase of our research program.

Figure 2.17 shows corresponding vertical and spanwise velocities at different phases during the cycle for a high amplitude case ($6V_{P-P}$). Here, the net effect is quite different from the low-amplitude case presented before. There is a clear attraction between the two jets, and their primary streams are bent towards each other, merging at the top of the measurement frame. However, due to the very small region that was measured, it is not clear how the overall structure of the dual jet develops further away from the wall. Smith *et al.* [21] show that adjacent jets do combine to form a single jet with increased strength, but that the formation is not complete until approximately $10 h$ from the wall - roughly the extent of the measurement domain in the current experiments. Thus, it is likely that a similar situation exists at this condition, but has simply not been fully characterized in the far field.

Figure 2.18 shows the near-field velocity fields for the case of two jets operating 180 degrees out of phase. Here, the operating conditions are $Re = 76.3$, $St = 40$, $Str = 0.786$. As before, one of the actuators (the right one) is operating at a slightly lower amplitude than its pair, and so the interaction is not as optimal as one might have hoped for. Nevertheless,

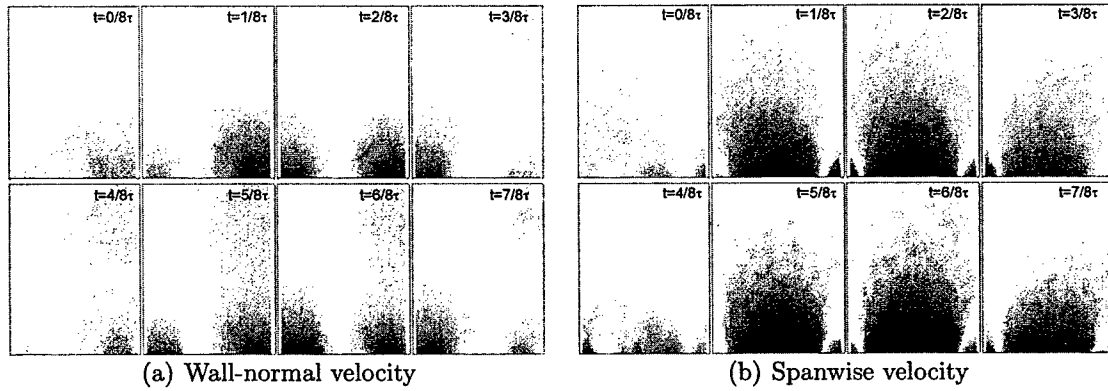


Figure 2.16: A velocity measurement of a pair of actuators operating out of phase (180°) at 60 Hz and with an input voltage of $1 V_{P-P}$. The dimensions, actuator location, and color mapping are the same as in Figure 2.15.

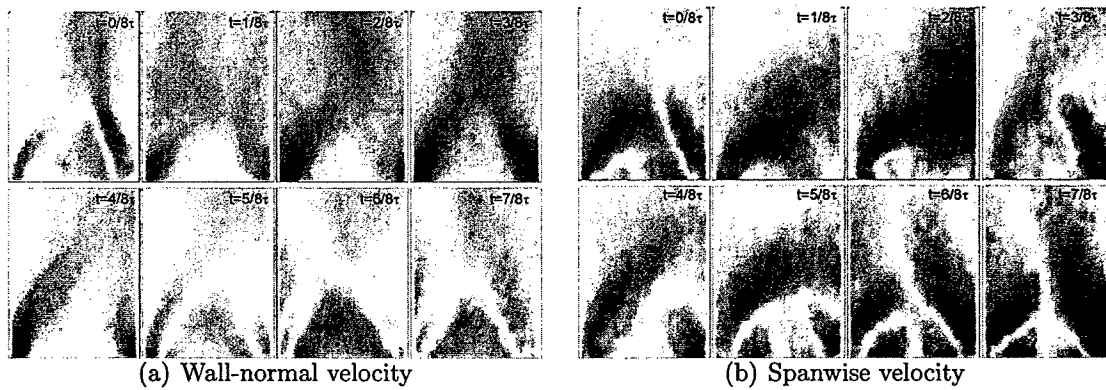


Figure 2.17: The wall-normal velocity at 8 phases of a pair of actuators operating in phase at $5 V_{P-P}$ and 60 Hz. The colors ranges from -8cm/s to 8cm/s . The dimensions and actuator location are the same as Figure 2.15.

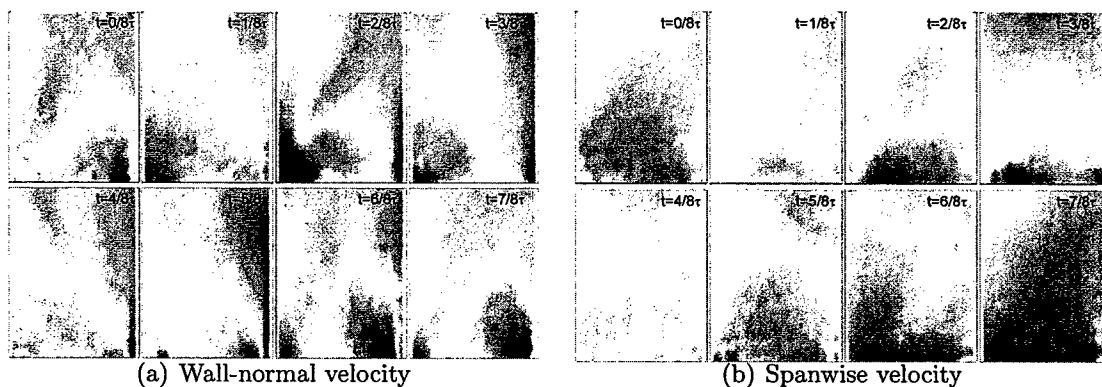


Figure 2.18: The wall-normal velocity of a pair of actuators operating out of phase at $5 V_{P-P}$ and 60 Hz. The dimensions and actuator location are the same as Figure 2.15. The colors ranges from -8cm/s to 8cm/s. The colors ranges from -4cm/s to 4cm/s. The dimensions and actuator location are the same as Figure 2.15.

the strong cooperative interactions are evident, and the broadening of the jet quite striking, even in this near field (compare the width of the streamwise velocity patterns in Figures 2.17 and 2.18).

The particular application of interest here - near wall turbulence control leads to an operating regime for the actuators which is somewhat different from the traditional applications in which synthetic jets have been used. Here, we are primarily interested in the near field of the actuator, and in operating the jets at relatively low Reynolds number and high Strouhal numbers. As a comparison, the adjacent jet work of Smith *et al.* [20] is in the Re 600, Str 0.03 range, while the current work is at $Re = 20 - 80$, $Str = 40$, Str 1. Nevertheless, similar effects are observed when studying the interactions between two synthetic jets operating in close proximity. At low amplitudes, where the jets are operating in their reversible mode, the net effect appears to be linearly additive, and there seems little interaction between the two systems (this still needs to be confirmed more carefully). However, at higher amplitudes, where the suction phase and distorted pressure field have much greater force and range, the effects are much more striking, and we see the jets distorted.

2.5.2 Open loop forcing in turbulent channel flow

The actuator array was installed into the water channel to measure the effect of open-loop forcing of the actuator on a turbulent flow. Figure 2.19 shows the mean streamwise velocity profile and the corresponding fluctuations of the channel flow. These profiles compare favorably to works by Kim, Moin, and Moser [9], and we can conclude that the turbulent flow is fully developed. Figure 2.20 is a measurement of the streamwise velocity of the flow directly over an actuator slit with no input signal. The center of the slit is positioned at the bottom left corner of the field of view, capturing the downstream half of the exit slit, as well as 10 mm ($125 l^*$) of the flow downstream of the actuator. Figure 2.20 shows that there are no large disturbances to the flow, so we can conclude that the slit opening is not contributing

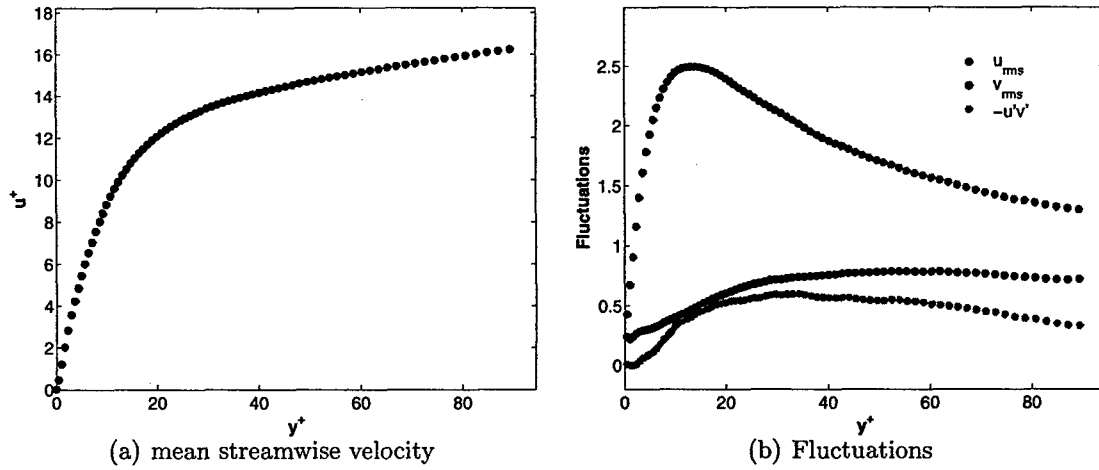


Figure 2.19: The baseline channel flow. Mean streamwise velocity is shown in (a). Fluctuations in (b) confirm that the turbulent flow is well-developed.

to any redirection of the flow.

With the actuators running, velocity measurements were taken at different spanwise locations in order to measure their effect on a turbulent channel flow. From Figure 2.12, which shows the actuator running at $5 V_{P-P}$ and 60 Hz in a water tank, we expect a region of upward motion over the slit and downward motion to the sides resulting from an irreversible jetting during the blowing phases. Under the same conditions, Figure 2.21 shows velocity measurements at four spanwise locations, starting from a distance $z^* = 50$ from the actuator and moving closer to the actuator. At $z^* = 50$, the flow appears unaffected by the actuator. In Figure 2.21(b), at $z^* = 34$, the downward influence of the actuator can be observed. The upward force of the actuator can be witnessed in Figure 2.21(c), at $z^* = 17$. The strongest blowing can be seen in Figure 2.21(d), at $z^* = 0$. These measurements confirm that the operation of the actuators maintain their irreversible flow characteristics when installed into a channel flow.

Figure 2.22 shows the streamwise velocity profiles of four cases taken at two voltages, $2 V_{P-P}$ and $5 V_{P-P}$, each at the phases coinciding with maximum blowing and suction. Also plotted is the baseline flow profile. The profiles are from the same field of view as Figure 2.21, averaged over the streamwise direction. The effect of the actuators running at the lower amplitude does not significantly affect the profile of the flow, indicating that the flow may be suppressing the actuator output. The higher amplitude, however, shows a significant effect, with a slowdown of the fluid caused by the upward jetting effect of the actuator. Also note that the phase of the actuator does not significantly alter the magnitude of the effect, which confirms that the region of upward motion is persistent throughout the operation cycle.

Additionally, measurements were taken using the shear stress sensors located downstream of the actuators. Figure 2.23 shows data taken to compare the changes in sensor voltage for various actuator amplitudes and frequencies. The change in voltage is defined as the difference of the sensor level at an actuated case from that at a baseline case divided by

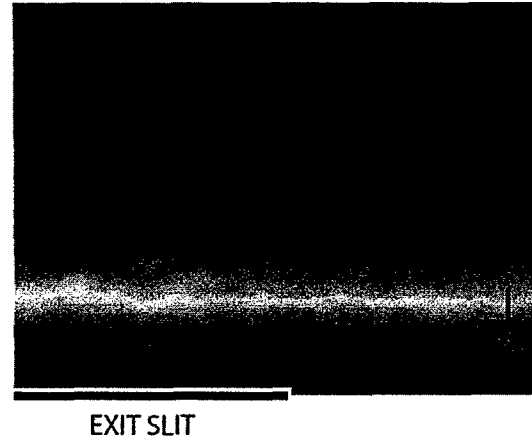


Figure 2.20: A PIV measurement streamwise velocity of the baseline channel flow. The colors ranges from 0 to 12cm/s($u^+ = 15$).

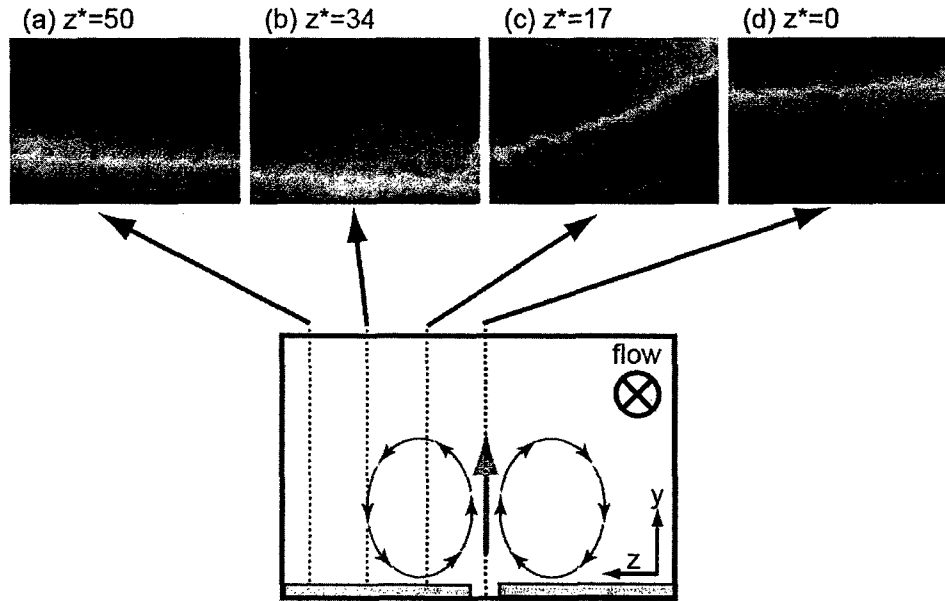


Figure 2.21: Figures (a) - (d) show streamwise velocity at various spanwise locations of the channel flow during actuator operation at $5 V_{P-P}$ and 60 Hz. Dimensions are identical to those of Figure 2.20. The colors range from 0 to 9cm/s. The inset is a schematic of the vorticity formed by the actuator.. Examining the different spanwise locations, the actuator has little effect on the channel flow at $z^* = 50$ (a), the downward portion of the synthetic jet can be seen at $z^* = 34$ (b). The upward momentum can be clearly seen at $z^* = 17$, (c), and $z^* = 0$, (d).

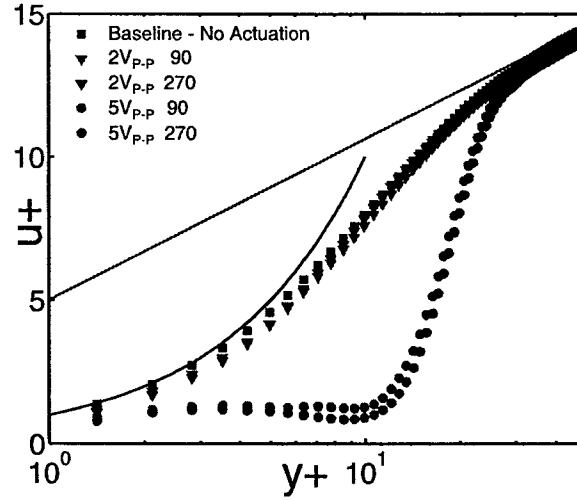


Figure 2.22: Velocity profiles of the channel flow comparing actuated and non-actuated cases averaged over the streamwise direction. The data is acquired from the field of view in Figure 2.20. The actuator effect can be seen and is largely dependant on amplitude. The actuator is pushing lower speed fluid upward. Note that the effect is largely independent of actuator phase.

the RMS of the sensor during a baseline case. Since the sensors could not be calibrated exactly, the RMS represents a normalizing value that scales the overall voltage change by the relative sensitivity of the sensor such that comparisons can be made between different sensors. Positioned $60 l^*$ downstream, the sensors were sampled at 250 Hz for 300 seconds. At voltages of $2 V_{P-P}$, there appears to be little change in the sensor voltage from the baseline, which agrees with the PIV data in Figure 2.22. However, at $4 V_{P-P}$, there is a significant negative deviation, indicating a reduction of the shear stress and indicating a slowing of the flow, which also agrees with the analysis of Figure 2.22.

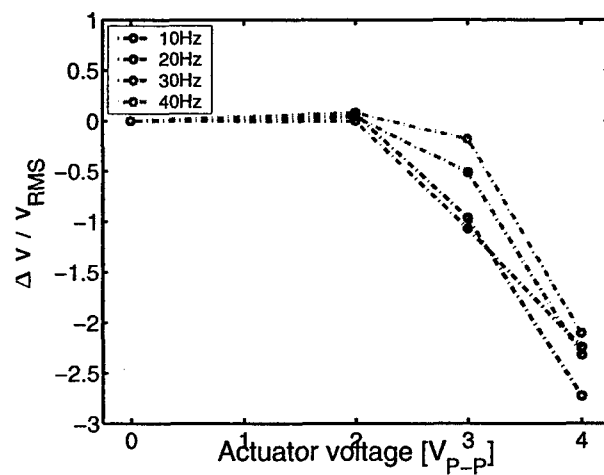


Figure 2.23: Shear stress measurements showing the downstream effect of the actuators at various voltages and frequencies. Negative deviations indicate a slowdown of the flow over the sensor.

Chapter 3

Control Theory

In this chapter, the development of a control scheme for the active management of shear layers in a turbulent flow is presented. Previous work by Rathnasingham and Breuer [14] has shown that we can assume the primary contributions of the dynamics near the wall evolve from coherent structures. Thus the controller is designed to function using shear sensor measurements at the wall. Since the dynamics of the actuators are not fully known and might change depending on flow conditions, an adaptive algorithm is required. The development of such an approach is presented in this chapter.

3.1 Finite Impulse Response (FIR) Filters

In order to understand the control theory, we must examine the goals of the experimental system and how it will go about achieving them. The control system uses data from wall-based sensors to determine variations in the shear stress and then attempts to minimize fluctuations by sending electrical signals to the actuators. Because the controller begins operating with little or no prior knowledge of the system, it also relies on feedback from the sensors located downstream to find how best to operate the actuators. Generally speaking, controllers rely on filters to extract information from noisy data. Filters used in discrete-time signal processing are classified into two categories, finite impulse response (FIR) and infinite impulse response (IIR). In FIR systems, the output is defined as a weighted average of a sequence of input data.

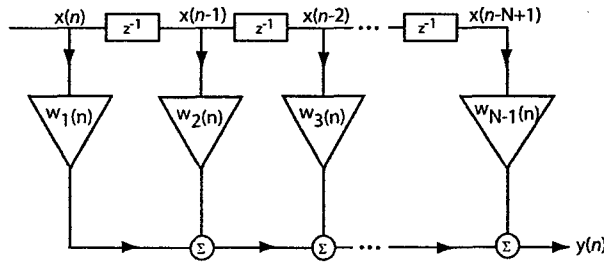


Figure 3.1: Conceptual view of FIR filtering as the weighted sum of past input values.

The implementation of the FIR filter can be expressed as the weighted sum of a finite number of these input data points :

$$y(n) = \sum_{k=0}^{N-1} a_k x(n-k), \quad (3.1)$$

where $x(n)$ is the system reference signal at time n and $y(n)$ is the output. This calculation can also be seen visually in Figure 3.1, where the z^{-1} blocks are unit delays. The impulse response of this system can be expressed as:

$$w(n) = \begin{cases} a_n, & 0 \leq n \leq N-1 \\ 0, & \text{otherwise} \end{cases}, \quad (3.2)$$

therefore the output can be written in terms of the impulse response, $w(n)$:

$$y(n) = \sum_{k=0}^{N-1} w(k)x(n-k). \quad (3.3)$$

Alternately, the FIR equation can also be expressed as a vector inner product:

$$y(n) = \mathbf{w}^T \mathbf{x}(n), \quad (3.4)$$

where T denotes the vector transpose and \mathbf{w} and $\mathbf{x}(n)$ are defined as:

$$\begin{aligned} \mathbf{w} &= [w(0), w(1), \dots, w(N-1)] \\ \mathbf{x}(n) &= [x(n), x(n-1), \dots, x(n-N+1)] \end{aligned} \quad (3.5)$$

The other type of filter in digital signal processing, the IIR, utilizes a transfer function with coefficients that are non-zero over an unbounded range. The output of the IIR filter can be defined as:

$$y(n) = \sum_{k=0}^{\infty} a_k x(n-k), \quad (3.6)$$

where the impulse response, $w(n)$, is defined as:

$$w(n) = \begin{cases} a_n, & 0 \leq n < \infty \\ 0, & n < 0 \end{cases}. \quad (3.7)$$

The choice of using FIR filters in these experiments was made based on the relative advantages of the two. First, FIR filters have a linear phase response so that no phase distortion is introduced by the filter. The phase response of IIR filters can be non-linear, especially at the band edges. Second, FIR filters are computed without any recursion, not true of IIR filters, and are always stable. The stability of IIR filters cannot be guaranteed. Hence, the FIR filter was chosen for its convenience of implementation and stability advantages.

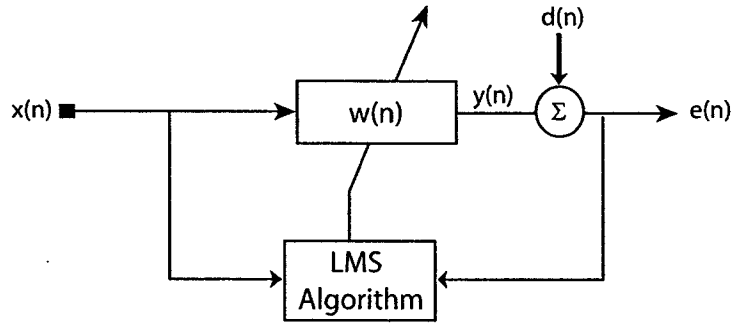


Figure 3.2: The LMS Algorithm requires data from both the input and the output to improve its performance.

3.2 Least-Means Squared (LMS) Algorithm

Previous work done by Rathnasingham and Breuer [16] successfully utilized an FIR filter in which the optimal filter coefficients were determined via system identification from the auto- and cross-correlation functions such that the time-averaged mean square error was minimized. The process was computationally intensive and vulnerable to environmental changes such as sensor drift and actuator performance changes. An adaptive algorithm that computes these coefficients, while adapting to environmental changes, would greatly improve the practicality of the control system. The LMS algorithm, first introduced in 1960 by Widrow and Hoff [22], is a linear adaptive filtering technique that relies on two principal processes, a filtering process and an adaptive process. The filtering process is an FIR filter that relies on the adaptive process to generate its transfer function coefficients. The adaptive process takes downstream data of the system and adjusts the filtering processing coefficients until a specified performance goal is reached. This layout defines a feedback loop[6].

As illustrated in Figure 3.2, the reference signal to the system is $x(n)$, while the output of the system is $y(n)$, $d(n)$ is the desired signal, and $e(n)$ is the error. For our application, $x(n)$ is the signal from the sensors located upstream of the actuators. As in equation 3.4, the output, $y(n)$, is the output of an FIR filter, defined as:

$$y(n) = \mathbf{w}^T(n) \cdot \mathbf{x}(n). \quad (3.8)$$

The error signal, $e(n)$, is defined as:

$$e(n) = d(n) - y(n). \quad (3.9)$$

We can see that the controller will continue to adjust the taps until $e(n)$ is zero. For our application of drag reduction, $d(n)$ acts as the desired downstream sensor output and if the controller is successful, the system attempts to minimize fluctuations once at that voltage level. The adaptive portion of the algorithm is defined in the coefficient update:

$$\mathbf{w}(n+1) = \mathbf{w}(n) + \mu x(n)e(n) \quad (3.10)$$

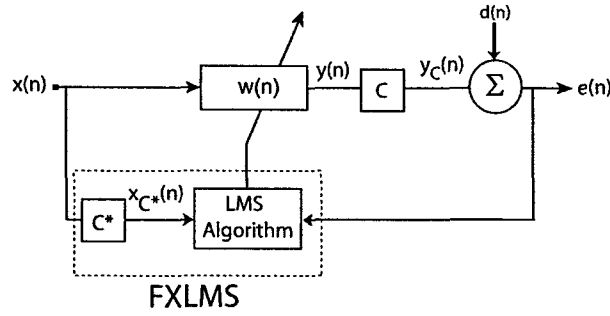


Figure 3.3: The Filtered-X LMS Algorithm compensates for the system dynamics, C , by adding an additional filter, C^* , to the input that approximates the dynamics of the system.

The adjustment factor, μ , dictates the magnitude of the changes to the coefficients at each time step. If μ is large, then the influence of the existing transfer function is lessened. Conversely, if μ is small, then changes to the coefficients are smaller. In this way, μ can be viewed as a measure of the algorithm's "reaction" to perturbations in the error signal since higher μ values will cause larger changes in the filter taps. μ must be chosen such that it is small enough that the control system converges accurately, but large enough that the system converges quickly.

3.3 Filtered-X LMS (FXLMS) Algorithm

The feedback loop of the LMS algorithm can be a source of instability [13, 6, 5], especially in applications that experience delays in the error path. If the error signal, $e(n)$, is out of phase with the reference signal, $x(n)$, the adjustments to the FIR filter coefficients do not accurately adapt to the external system. The Filtered-X LMS algorithm addresses the issue of phase delays in the error path by introducing a filter to the reference signal. Illustrated in Figure 3.3, two filter blocks have been added to the LMS system. The filter with transfer function C , represents the dynamics of the channel flow and can include the time delay indicative of fluid propagation, nonlinearities in the flow, or measurement noise. In order to compensate, another filter, with transfer function, C^* , is introduced into the forward path of the system. The transfer function C is defined by the environment and filter C^* serves as an estimate. Ideally, the estimate is determined by finding the impulse response of the system, but success has been demonstrated by simply implementing a proper phase delay [13, 6, 5].

While Equation 3.8 still applies, the error signal to the filter becomes:

$$e(n) = d(n) - y_C(n), \quad (3.11)$$

where the output $y_C(n)$ is defined as:

$$y_C(n) = C \cdot y(n), \quad (3.12)$$

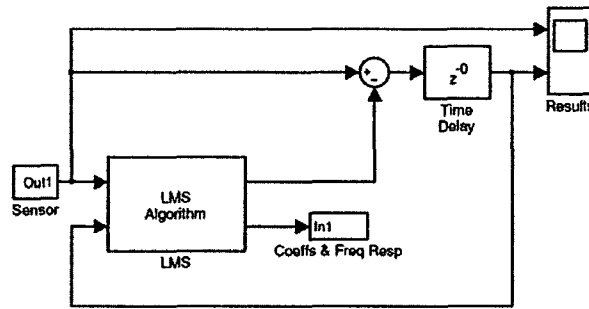


Figure 3.4: The LMS system was implemented using MATLAB Simulink.

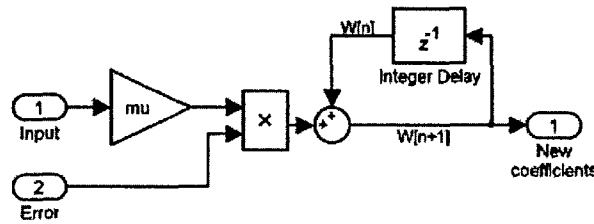


Figure 3.5: The LMS portion of the simulation is shown.

where $y(n)$ is now a data sequence and the new reference signal, $x_{C^*}(n)$ is defined as:

$$x_{C^*}(n) = C^* \cdot x(n), \quad (3.13)$$

and the adaptation routine becomes:

$$w(n+1) = w(n) + \mu x_{C^*}(n) \cdot e(n). \quad (3.14)$$

3.4 MATLAB Simulation of Control System

MATLAB was used to test the performance of the control system. MATLAB's Simulink environment is a graphical simulation environment that can be used for a wide range of experiments. In order to test the LMS and FXLMS algorithms, noise sources and simulated plants were introduced to estimate the actual behavior of the channel flow.

The LMS algorithm, pictured in Figure 3.4, was tested first as it was the basis for the FXLMS system. A noise cancellation demo included with MATLAB utilizes an LMS block (Figure 3.5) and was used for these simulations. The number of coefficients, or taps, are variable, as is μ , the adjustment weight. The "Sensor" block on the left contains a repeatable Gaussian noise source summed with a sine wave generator. The output of the LMS block is subtracted from the original signal and the error signal is fed back.

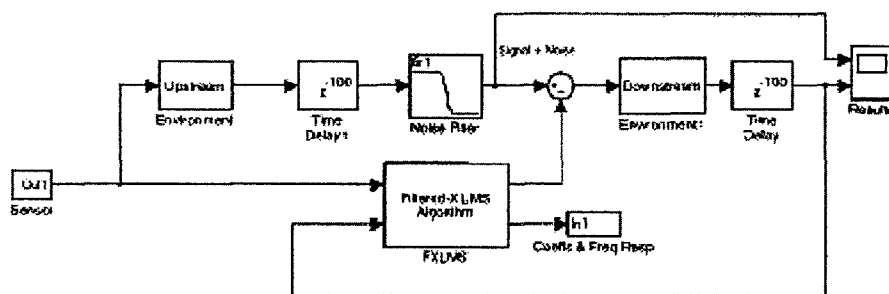


Figure 3.6: Simulink Simulation of a 1-channel FXLMS filter

In order to implement an FXLMS filter, modifications to the MATLAB LMS filter were required. Paths to the FIR filter and the adaptive algorithm are independent, as the input to the adaptive process is filtered by the simulated forward path and the FIR filter operates on the real-time input data (Figure 3.6).

Further, a multichannel version of the FXLMS was designed to improve the performance of the controller by minimizing the impact of nonlinearities caused by turbulence or measurement noise. An FXLMS system utilizing two upstream sensors and a single downstream sensor is shown in Figure 3.7. The system is effectively 2 parallel processes, receiving input signals from two different noise sources and performing separate FIR calculations, however they both contribute to a single actuator and receive a single error signal. The output of the FIR filters are then averaged to generate one output signal. For our simulations, outputs from both processors are averaged and subtracted from a signal composed of the two independent source signals.

To further gauge the flexibility of the FXLMS routine and better model a turbulent flow, the simulation was modified. A delay buffer was added to the upstream path of the system (Figure 3.8). Also, a subsystem was developed to introduce signal nonlinearities into the simulation. Pictured in Figure 3.9, the signal is first processed by a discrete-time derivative block and then squared. The output of the nonlinear path is then summed with the original signal. The magnitudes of both the linear and nonlinear component are variable.

3.4.1 DSP Code

DSPs were programmed with the adaptive updating routine once the simulations proved the feasibility of applying the FXLMS algorithm to this flow control case. The size and sampling rate of the filter is dictated by the number of FIR calculations needed to successfully generate actuator signals. The estimated delay was determined from the approximate propagation time between the actuator and sensors. At a velocity of $10 u_\tau$, and covering a distance of $250 l^*$, the delay should be on the order of $t^* = 25$, or roughly 0.40 seconds. The DSPs were able to run a 500-tap filter at 250 Hz for three upstream sensors and one error signal, as shown in Figure 3.10, well within the design constraints. The system was run in a controlled environment using wave generators before being installed in the flow facility.

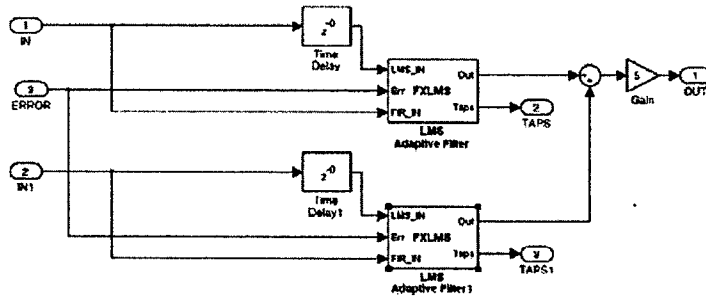


Figure 3.7: The multichannel FXLMS. Note that there is only one error signal and one output signal.

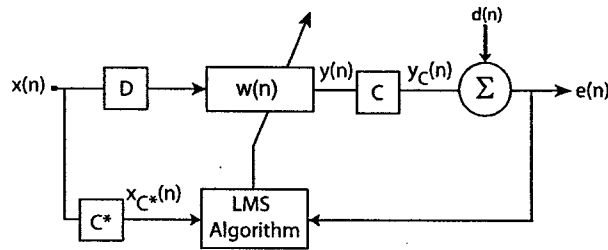


Figure 3.8: In addition to the error path response, there are phase delays in the reference signal path, in our case the flow dynamics between the upstream sensors and the actuator.

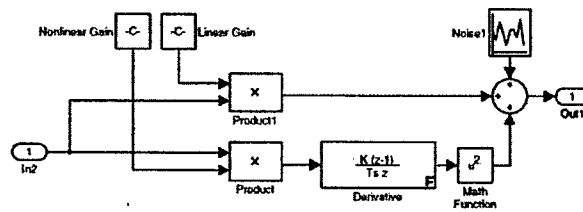


Figure 3.9: The environment block used to simulation the nonlinearities of the turbulent flow.

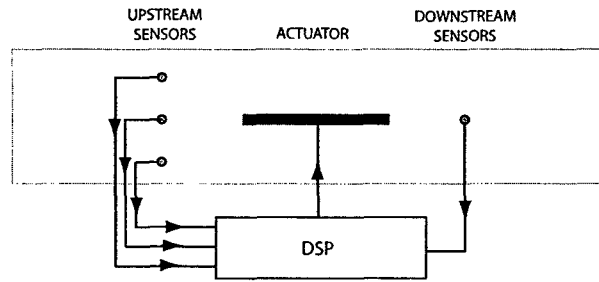


Figure 3.10: The product of the simulation phase of the experiment was a DSP programmed to receive input from three upstream sensors and one downstream sensor to control each actuator.

3.5 Control System Performance

The Simulink results presented in this section outline the development of the FXLMS algorithm for the application of turbulent shear flow control. Figure 3.11(a) shows the performance of the LMS filter operating on a noise source composed of a sine wave of amplitude $2 V_{P-P}$ and Gaussian noise of variance $1 V$, both with a mean of $0 V$. The RMS of the error signal, the difference between the input signal and LMS filter output, is shown for a 64-tap filter operating at eight varying values of μ . The RMS is calculated using a moving 500-sample window. We use the RMS of the error signal as a gauge for the filter's success at removing fluctuations from the input. Examining the figure, we see that the LMS filter, operating with the smallest adjustment factor, $\mu = 0.01$, successfully reduces the variance of the input signal, albeit slowly. As μ increases the algorithm becomes faster in adapting to the input signal demonstrated by the steeper slope of the RMS. At $\mu = 0.5$, the filter converges the fastest. As μ increases past this value, the rate at which the output converges decreases until $\mu = 2.1$, at which point, the RMS increases dramatically, indicating that the control system is actually a detriment to the goal of noise attenuating. The behavior of the error can be expressed as:

$$E_{RMS} = Ae^{-\lambda t}, \quad (3.15)$$

where λ is the rate of adaptation, ie. the slope of the line in Figure 3.11(a), and A is a scaling factor. Figure 3.11(b) shows the effect of the adjustment factor, μ , on the rate of adaption, λ .

While the performance of the LMS system is dependent on μ , it is extremely vulnerable to delay in the error path. Figure 3.12 demonstrates the response of the LMS filter as the delay is set to increasing values using $\mu = 0.1$. With an error path delay of only two samples, the system is unstable and the instability grows rapidly as the delay increases to three samples. From Figure 3.11, we know that $\mu = 0.5$ results in the fastest convergence, but the system is most vulnerable to delay when running at that mode and becomes unstable with a delay of only one sample. As the μ factor is decreased, the instability caused by downstream delay can be prevented, but the settling time consequently increases. The FXLMS system allows

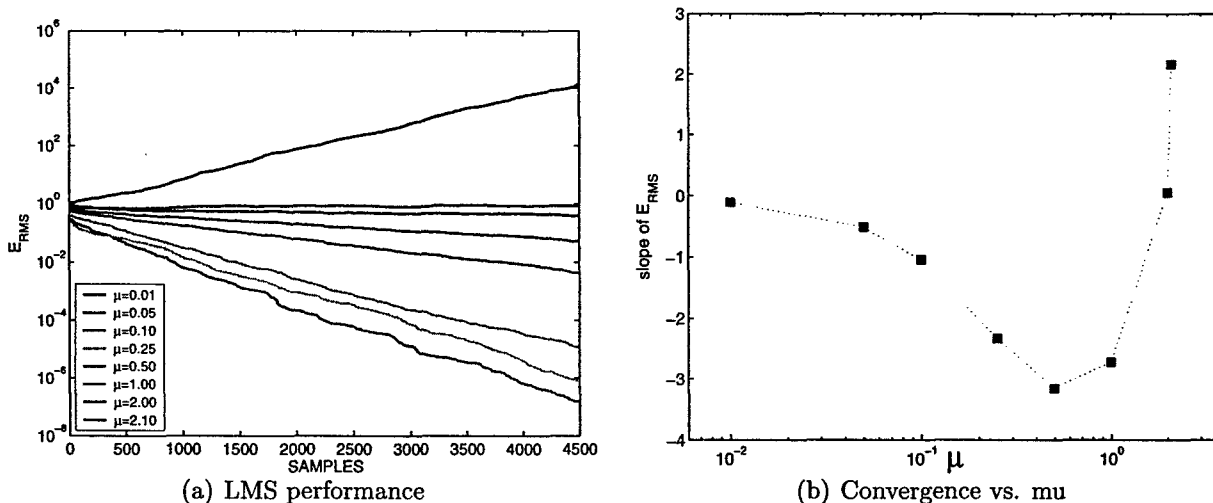


Figure 3.11: The performance of the LMS simulation with a combination Gaussian and sine wave inputs with a range of μ values. Starting at $\mu = 0.01$, the RMS does not change significantly since the coefficient adjustments are very small. As μ increases, the RMS decreases until $\mu = 0.5$, and then the performance worsens until $\mu = 2.1$, when the RMS increases from its initial value.

for stability in this case without the compromise in resolution time.

Figure 3.13 shows the FXLMS system successfully filtering the input signal when operating with the same error path delays as Figure 3.12. The source signal and the filter parameters are identical, but the reference signal is delayed by the same length as the downstream effect. Additionally, the figure shows a case where the downstream delay is 50 samples and the filter is able to adapt equally well.

The effect of the location of delays, however, were examined more closely. While the downstream delay does not significantly affect the performance of the control system assuming an accurate forward-path estimation, the upstream delay, the lag between the reference signal and the actuator summation, plays a role in the ability of the system to fully adapt to the external flow. Using the same input signal as the previous cases, in Figure 3.14 we can see the RMS of the outputs of the control system over time when dealing with various upstream delays. The filter was again a 64-tap filter with $\mu=0.1$. Note that as the delay approaches 50 samples, the controller is no longer able to attenuate the input. Examining the taps themselves reveals that the filter adapts to upstream delay by shifting the coefficients to "line up" with the system. As the delay approaches 50 samples, the filter is no longer able to filter noise because there are no longer enough "useful" taps to reconstructed the noise signal.

Figure 3.15 demonstrates the effect of the nonlinear subsystem on the performance of the FXLMS algorithm. As the relative magnitude of the nonlinear system increases, the final RMS of the error signal increases. However, in the case of multiple input channels, fluctuations in the error decrease as the number of channels increases. For this reason, the

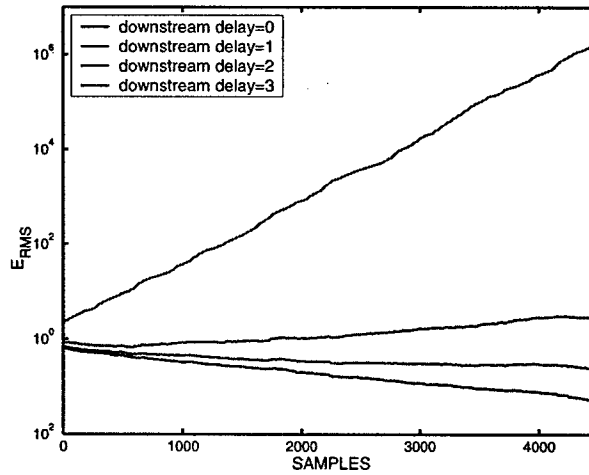


Figure 3.12: The stability of the LMS algorithm is vulnerable to delays in the error path.

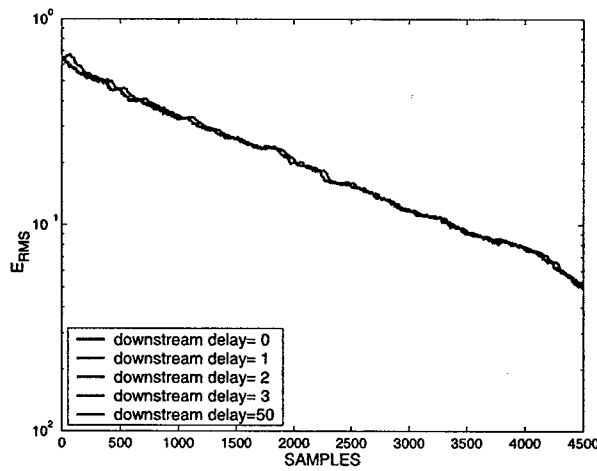


Figure 3.13: The 500-sample RMS of the error signal of the FXLMS MATLAB simulation, using the same input signal and filter variables of $\mu = 0.1$ and 64 taps, with downstream delays of 0, 1, 2, 3, and 50 samples. The FXLMS is successful in adapting to all of the cases.

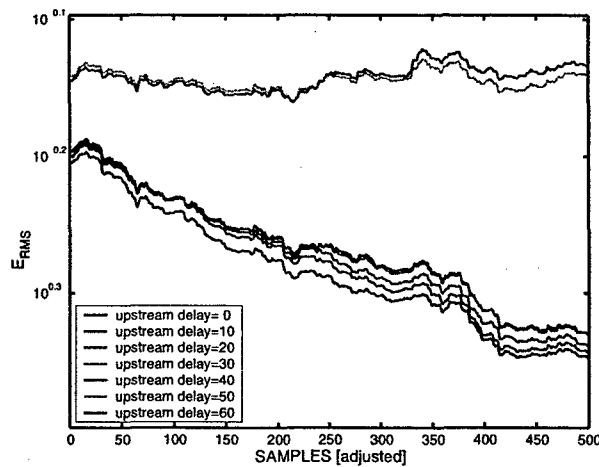


Figure 3.14: The effect of delays between the upstream sensor on the performance of the algorithm. Note that for delays of 50 and 60 samples, the filter is unable to filter the noise signal. The 64-tap filter does not have the capacity to store the delay and the necessary coefficients.

controller of the physical system was designed to input multiple inputs. For an array of four actuators, six upstream sensors and four downstream sensors were employed so that each actuator controller would acquire data from three upstream sensors and one downstream sensor.

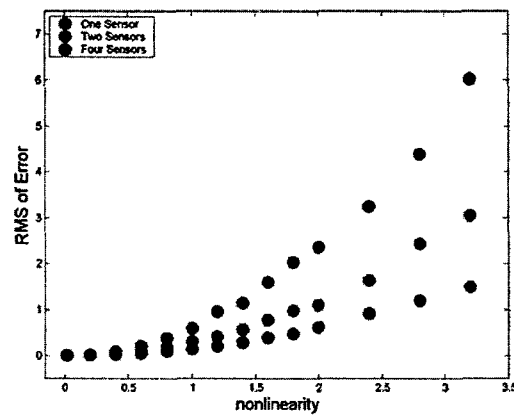


Figure 3.15: The effect of simulated system nonlinearities on the RMS of the error output. The system grows more unstable as nonlinearity increases. However, as the number of channels is increased, the variance of the system error (output) is decreased.

Chapter 4

Conclusions

The implementation of an array of synthetic jet actuators and an adaptive control algorithm for active flow control have been presented. The specific operation of the actuators was somewhat different from the “traditional” applications in which synthetic jets have been used. The jets operate at relatively low Reynolds number and high Strouhal numbers. Nevertheless, similar effects are observed when studying the interactions between two synthetic jets operating in close proximity. At low amplitudes, where the jets are operating in their reversible mode, the net effect appears to be linearly additive, and there seems little interaction between the two systems. However, at higher amplitudes, where the suction phase and distorted pressure field have much greater force and range, the effects are much more striking, and we see the jets distorted. The actuators also demonstrated strong, controllable forcing on a turbulent channel flow. The actuators seem to be well suited to the application of active flow control.

The Filtered-X LMS algorithm is an adaptive control theory that appears to be suitable for control of shear flows in a turbulent water channel. In our simulations, the time delay resulting from the propagation of fluid has been shown to cause instability in a basic LMS system. The FXLMS was simulated and demonstrated its ability to successfully identify the random input signals despite the presence of phase delays. The importance of carefully choosing the μ value and the length of the filter were presented. The use of a multichannel FXLMS has been shown to decrease the controller’s susceptibility to measurement noise and nonlinearities in the inputs.

The next phase of the research is to extensively measure the performance of the control system operating on a fully turbulent channel flow.

Bibliography

- [1] T. Bewley, P. Moin, and R. Temam. DNS-based predictive control of turbulence: an optimal benchmark for feedback algorithms. *J. Fluid Mech.*, 447:179–225, 2001.
- [2] R. F. Blackwelder. Hot wire and hot film anemometers. *Methods of Experimental Physics*, 18, 1981.
- [3] H. Choi, P. Moin, and J. Kim. Active turbulence control for drag reduction in wall-bounded flows. *J. Fluid Mech.*, Vol. 262:75–110, 1994.
- [4] A. Glezer and M. Amitay. Synthetic jets. *Ann. Rev. of Fluid Mech.*, 34:503–529, 2002.
- [5] L. Hakansson. The filtered-x lms algorithm. University of Karlskrona/Ronneby.
- [6] S. Haykin. *Adaptive Filter Theory*. Information and System Sciences Series. Prentice Hall, 4th ed. edition, 2002.
- [7] M. Honohan, M. Amitay, and A. Glezer. Aerodynamic control using synthetic jets. AIAA Paper 2000-2401, 2000.
- [8] U. Ingard. On the theory and design of acoustic resonators. *J. Acoustical Soc. of America*, 25(6):1037–1060, 1953.
- [9] J. Kim, P. Moin, and R. Moser. Turbulence statistics in fully developed channel flow. *J. Fluid Mech.*, 177:133–166, 1987.
- [10] C. Lee and D. Goldstein. DNS of microjets for turbulent boundary layer control, 2001. AIAA Paper 2001-1013.
- [11] C. Lee and D. Goldstein. Two-dimensional synthetic jet simulation. *AIAA J*, 40:510–516, 2002.
- [12] D. C. McCormick. Boundary layer separation control with directed synthetic jets. *AIAA Paper 2000-0519*, 2000.
- [13] P. Nelson and S. Elliot. *Active Control of Sound*. Academic Press, 1992.
- [14] R. Rathnasingham. System identification and active control of a turbulent boundary layer. *PhD. Thesis, Department of Aeronautics and Astronautics, MIT*, 1997. (Also MIT FDRL Report 97-6).

- [15] R. Rathnasingham and K. S. Breuer. System identification and control of turbulent flows. *Phys. Fluids*, 9(7):1867–1869, 1997.
- [16] R. Rathnasingham and K. S. Breuer. Active control of turbulent boundary layers. *J. Fluid Mech.*, 2002. In Press.
- [17] A. Seifert, S. Eliahu, D. Greenblatt, and I. Wygnanski. Use of piezoelectric actuators for airfoil separation control (TN). *AIAA J.*, 36(8):1535–1537, 1998.
- [18] A. Seifert and L. G. Pack. Oscillatory control of separation at high reynolds numbers. *AIAA J.*, 37(9):1062–1071, 1999.
- [19] B. Smith and A. Glezer. The formation and evolution of synthetic jets. *Phys. Fluids*, 10(9):2281 – 2297, 1998.
- [20] B. Smith and A. Glezer. Jet vectoring using synthetic jet actuators. *J. Fluid Mech.*, 458:1–34, 2002.
- [21] B. L. Smith, M. A. Trautman, and A. Glezer. Controlled interactions of adjacent synthetic jets. AIAA Paper 99-0669, 1999.
- [22] B. Widrow and M. Hoff. Adaptive switching techniques. *IRE WESCON Conv. Rec.*, 4:96–104, 1960.